PAPER

Carboxy-silane coated iron oxide nanoparticles: a convenient platform for cellular and small animal imaging†

Dimitri Stanicki,[a] Sébastien Boutry,[b] Sophie Laurent,[a] Ludivine Wacheul,[b] Emilien Nicolas,[bc] Deborah Crombez,[a] Luce Vander Elst,[a] Denis L. J. Lafontaine*[bc] and Robert N. Muller*[ab]

This study reports the synthesis of stabilized ultrasmall iron oxide nanoparticles (USPIO) as bimodal probes for magnetic resonance and optical imaging. These nanosystems are based on small iron oxide cores surrounded by a thin polysiloxane shell exhibiting carboxylic acid functions. Thanks to these functions, hybrid particles were obtained by conjugating a fluorophore to the superparamagnetic contrastophore. Such modification allowed us to directly follow these USPIO *in cellulo*, which provided interesting information about their internalization pathway and cellular distribution upon mitosis. Finally, the efficiency of these systems as probes for bimodal imaging was emphasized by the observation of their *in vivo* behavior in mice using magnetic resonance and optical imaging.

Introduction

Superparamagnetic iron oxide nanoparticles including magnetite (Fe_3O_4) and its oxidized form maghemite (γ-Fe_2O_3) exhibit a wide scope of applications extending from mechanics to medicine. In the biomedical field,[1–4] their use in cell recognition and separation, drug delivery, or hyperthermia is now well established. In magnetic resonance imaging (MRI), thanks to their great influence on proton relaxivities, such nano-systems have been widely used for liver and spleen imaging as well as for USPIO-marked cell tracking.

Whatever be the application, the stability of these nano-objects under physiological conditions is one of the key factors for their use as probes or as vectors in biological environments. Many strategies have already been considered in order to prevent particle aggregation. Typically, a repulsive force can be created between the systems by surrounding them with a steric or electrostatic crown.[5–7] Among the different approaches already considered, we can cite the post-addition of water-soluble ligands, including, among others, direct adsorption, addition of a second layer, ligand exchange, ionic interaction, or functional silica coating.[8–16] Ideally, the coating material should

be biocompatible, interact strongly with the nanoparticle surface, and exhibit functional groups which allow further conjugation. In this context, surface modification with organosilanes emerges as an interesting approach. Organosilanes are bifunctional molecules having the general formula $X–(CH_2)_n–Si(OR)_n$, where X is a functional group and $–Si(OR)_n$ are anchoring groups that allow a covalent bond between the silane and the inorganic surface through the formation of a strong SiO–M bond (M being a metal substrate). In the present study, USPIO stability has been reached after treatment with 3-(triethoxysilyl)propylsuccinic anhydride (TEPSA) by using a simple coating protocol that ensures the formation of a thin carboxylated layer of polysiloxane.[17]

In addition to the benefits of an electrostatic stabilization, the presence of carboxylic functions opened the door to the covalent tagging of the nano-platform in order to improve its performance. As a prototype, we decided to combine a fluorescent compound to the synthesized MRI platform. Such modification allowed us to follow directly these USPIO *in cellulo*, providing interesting information about their internalization pathway and cellular distribution upon mitosis.

Finally, the performance of the as-prepared nano-system as a potential probe for bimodal imaging was evaluated in a mouse model by studying USPIO distribution by magnetic resonance and optical imaging.

Results and discussion

Synthesis and characterization of the bimodal probe

As depicted in Fig. 1, four steps were necessary for the elaboration of such a bimodal system. The iron oxide cores were

[a]Department of General, Organic and Biomedical Chemistry, NMR and Molecular Imaging Laboratory, University of Mons, B-7000 Mons, Belgium. E-mail: robert.muller@umons.ac.be

[b]Center for Microscopy and Molecular Imaging, B-6041 Gosselies, Belgium

[c]Laboratory of RNA Metabolism, Brussels, Belgium. E-mail: denis.lafontaine@ulb.ac.be

This journal is © The Royal Society of Chemistry 2014

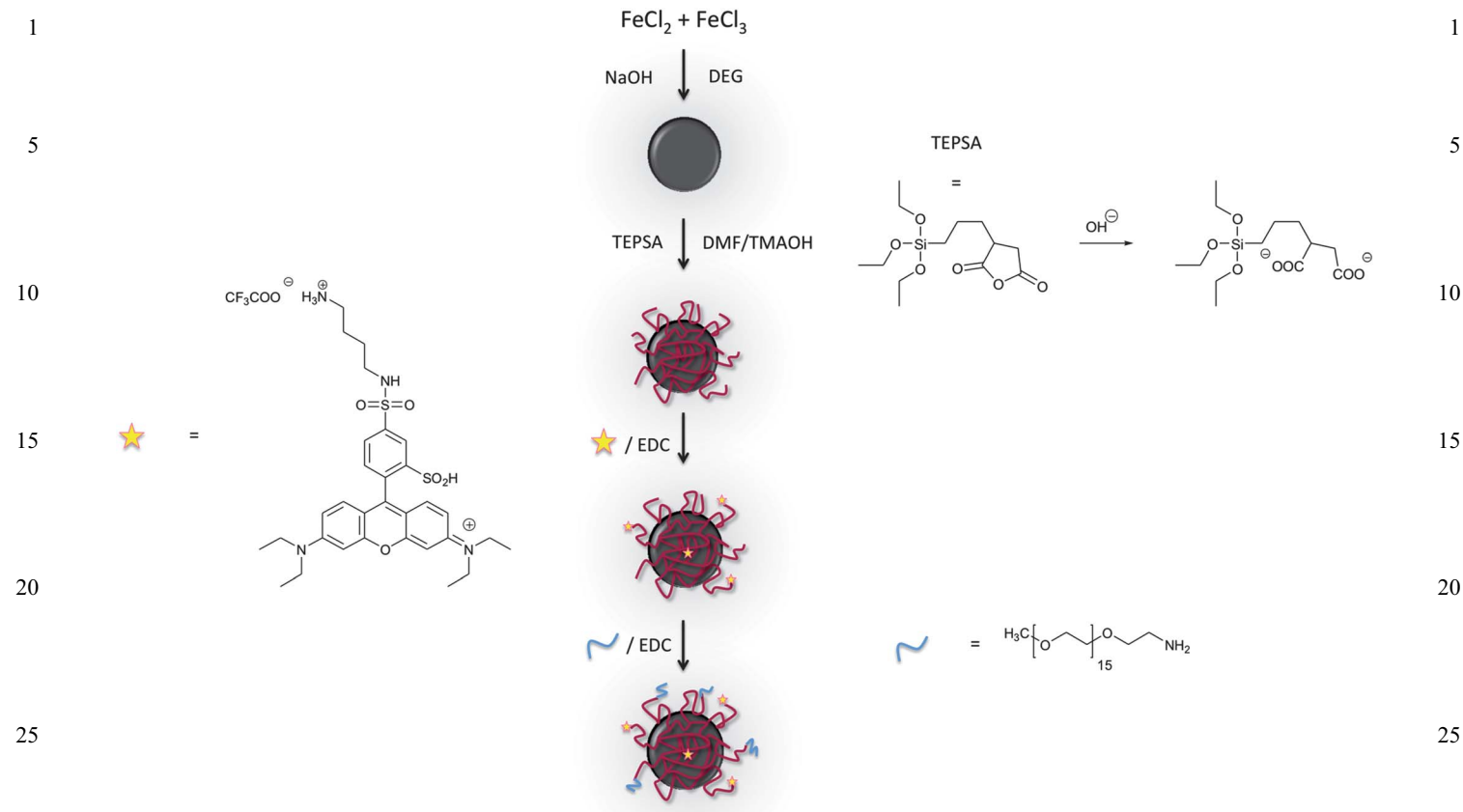*J. Mater. Chem. B*, 2014, **xx**, 1–11 | 1

Fig. 1 Synthetic route to obtain the proposed bimodal probe: step 1, co-precipitation of iron salts in basic organic medium; step 2, stabilization of the iron oxide cores by means of TEPSA treatment; step 3, tagging of the particle surfaces by a fluorescent molecule (denoted by a star); and step 4, PEGylation of the nano-systems.

prepared by a well-established method of co-precipitation of iron salts in DEG.[22] In addition, to allow the easy transfer of the nano-objects in water, the use of DEG leads to a significant reduction of the particle size distribution in comparison to the classical co-precipitation method. Photon correlation spectroscopy (PCS; Fig. S1†) as well as transmission electron microscopy (TEM; Fig. 2) confirmed the formation of well-dispersed nano-structures characterized by a small polydispersity index (1.31 by TEM and 0.102 by PCS). The mean core diameter determined by TEM was evaluated to be 7.8 nm.

To ensure the colloidal stability of the nano-systems, the use of organofunctional silanes has been preferred to other more conventional polymeric matrices.[23–25] USPIO stabilization by means of organosilane coating is of special interest mainly because of the biocompatibility of silica[26] and thanks to the formation of a stable Fe–O–Si covalent bond. Moreover, the great choice of commercially available organosilanes offers the possibility to covalently tag molecules of interest. In this work, TEPSA (Fig. 1) was chosen as a stabilizing matrix for our system. This molecule exhibits, after hydrolysis, the carboxylic functions necessary for stabilization and further conjugation. The surface modification by silanization is a quite complex process[27,28] depending on experimental parameters such as reaction temperature, silane concentration, pH, or solvent nature. To have better control of the hydrolysis of silane alkoxy

groups, the reaction was performed in organic medium in the presence of a controlled amount of water, as previously described.[17] After thermal treatment, the obtained particles can be easily dispersed in water at physiological pH, confirming the process efficiency. PCS measurements (Fig. S1†) revealed a slight increase of the hydrodynamic diameter (16.4 nm for bare NPs and 18.8 nm for TEPSA-coated NPs) and no enlargement of the size distribution, suggesting, first, the formation of a thin layer surrounding the NPs and, second, the coating of individual objects. In both cases, the presence of a single population characterized by a quite narrow size distribution could be identified, as was also observed by TEM (Fig. 2). Zeta potential measurements (Fig. S2A†) and FTIR spectroscopy (Fig. S2B†) completed the characterization and confirmed the presence of the expected shell.

As mentioned earlier, in addition to the advantage of an electrostatic stabilization, the presence of carboxylic functions allowed the introduction of a fluorescent probe, namely rhodamine (Fig. 1), in order to combine into the MRI tracer the benefits of optical imaging.

Prior to conjugation, rhodamine sulfonyl chloride was derivatized by introducing a butylamine linker in a two step reaction involving, first, the nucleophilic displacement of chloride in lissamine by the unprotected amine of N-Boc-1,4-butanediamine, followed by the amine deprotection in acidic
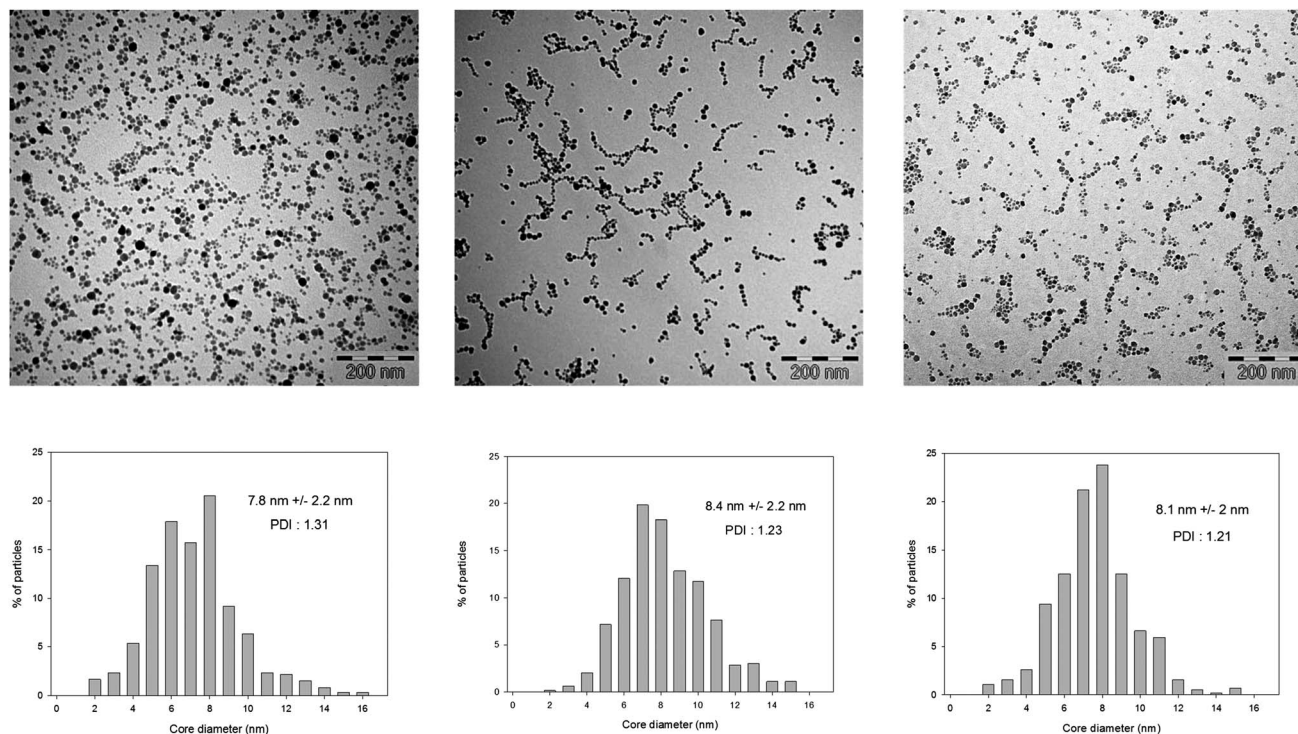
Fig. 2 TEM pictures of the nanoparticles obtained *via* the polyol route (left), of the TEPSA-coated NPs (middle), and of the TEPSA–Rh-NPs (right). The size distribution was obtained after a count of more than 500 particles. PDI: polydispersity index.

medium. The as-synthesized compound was covalently grafted to the USPIO surface by using EDC as a coupling agent. Ungrafted molecules were eliminated by membrane filtration until no fluorescence could be detected in the supernatant.

Despite the good stability of the TEPSA-coated NPs, we observed that the introduction of the rhodamine derivative on the NP surface induced a slow destabilization (*i.e.* several hours after the purification steps) of the colloidal suspension. To avoid any agglomeration, short polyethyleneglycol chains (MW = 750 g mol^{-1}) were introduced into the reaction media and covalently grafted to the NP surface in order to cap the remaining carboxylate functions.

The presence of fluorophores at the USPIO surface was attested by fluorimetric spectroscopy and optical imaging (Fig. S3†). In fact, contrary to TEPSA-coated USPIO, the hybrid system (TEPSA–Rh–PEG NPs) exhibited a strong emission signal after excitation at 540 nm in an optical imaging analysis. Assuming that iron oxide cores are monodisperse and spherical, we estimated by fluorimetric spectroscopy quantitation the amount of fluorophore grafted onto the USPIO surface to be approximately 3 molecules per particle (considering 8 nm particles). These data are in good agreement with the results obtained by Rerat *et al.*[29] who estimated the number of grafted RGD peptidomimetics per particle to be approximately 2.7.

Nuclear magnetic resonance dispersion (NMRD; Fig. 3) profiles were obtained in order to compare the relaxometric properties of TEPSA-coated NPs and TEPSA–Rh–PEG NPs at physiological pH and 37 °C. The poor stability of uncoated systems did not allow us to perform the corresponding analysis.
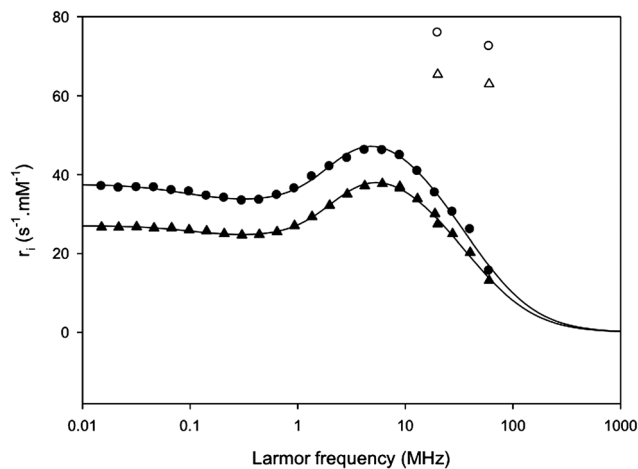

Fig. 3 Comparison of the NMRD profiles obtained for TEPSA-coated NPs (circles) and TEPSA–Rh–PEG NPs (triangles). Longitudinal relaxivities (r_1) are represented by filled forms and transverse relaxivities (r_2) by empty ones.

For both nano-systems, NMRD profiles show the typical curve expected for superparamagnetic NPs. Moreover, the small dispersion between 0.1 and 1 MHz and the small r_2/r_1 ratios at 1.41 T indicate that both systems were well dispersed, confirming the absence of aggregates, which is in agreement with the PCS measurements (Fig. S1†). A slight decrease of the relaxometric properties was also observed as a result of PEG treatment. This decrease of efficiency is consistent with the

This journal is © The Royal Society of Chemistry 2014

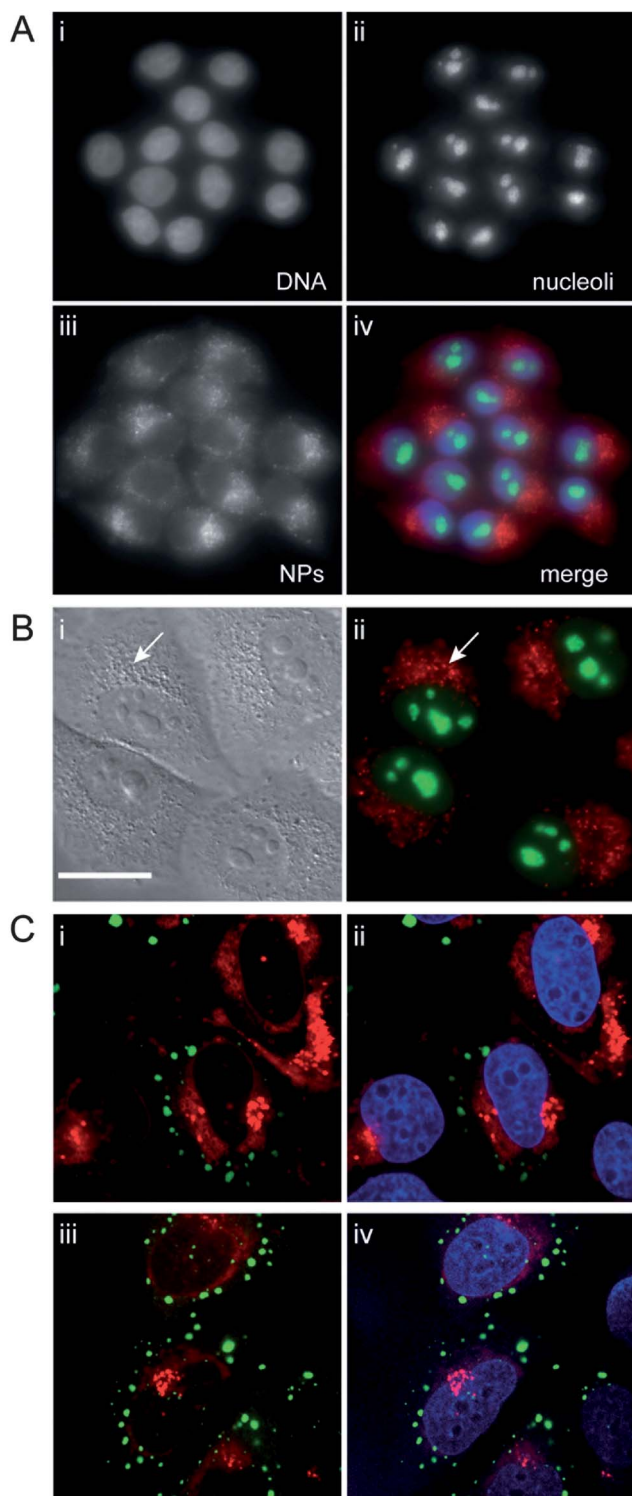*J. Mater. Chem. B*, 2014, **xx**, 1–11 | 3

Fig. 4 Vectorized NPs are naturally captured by cultured human cells and accumulate in cytoplasmic perinuclear foci. Intracellular distribution of TEPSA–Rh–PEG NPs analyzed by epifluorescence (A and B) and confocal (C) microscopy. Cultured HeLa or U2OS cells were incubated for 2 days with 50 μg Fe ml^{-1} equivalent of NPs, as described in the Experimental section. (A) HeLa cells stably expressing fibrillarin–GFP. Following fixation, cells were labeled with DAPI to highlight DNA (i). The nucleoli (ii) and the NPs (iii) appear in green and red, respectively, in the overlay section (iv); the DNA is in blue. Images acquired at 63× with a mercury illuminator and a Zeiss AxioCam HRm camera. (B) The same sample as in (A) imaged at higher resolution (100×) with a

increase of the shell thickness observed by PCS (6 nm between bare NPs and TEPSA–Rh-NPs).

Evidence of the colloidal stability of the as-prepared system was assessed by measuring the evolution of its longitudinal (r_1) and transverse (r_2) relaxivities at 1.41 T for a sample diluted (1 mM in iron) in physiological serum. The clustering of several magnetic cores usually leads to an increase of the r_2/r_1 ratio that can reach values up to several hundreds at high magnetic fields (Larmor frequency). The data indicated no evolution of this ratio (Fig. S4†), suggesting thus a good colloidal stability of the as-prepared nano-systems.

Cellular study

Given the fluorescence properties of the as-prepared USPIO, we were interested to find out whether such particles are naturally captured by cells in culture medium and, if so, to characterize their subcellular distribution. As a first approach, HeLa cells were incubated with a range of concentrations of vectorized NPs (0–300 μg Fe ml^{-1}) for 2 days. After the period of incubation, we confirmed that TEPSA–Rh–PEG NPs were indeed efficiently internalized within cells (Fig. S5† and data not shown). We found that the total fluorescence intensity corresponding to NPs increased steadily and quite linearly between 20 and 100 μg Fe ml^{-1} of NPs; however, we noted that above 60 μg Fe ml^{-1} the nano-systems showed a tendency to aggregate. In all further experiments, we used 50 μg Fe ml^{-1} as a working concentration as it provided a good compromise between a sufficient level of fluorescence and the absence of particle aggregation. Moreover, no significant effect on cell viability was detected after the incubation of HeLa cells with 50 μg Fe ml^{-1} of NPs over a period of 6 days (viable cells counted at 24 h interval, in a classic trypan blue assay, Fig. S6†).

We investigated the intracellular distribution of USPIO in both HeLa and U2OS cells. For co-localization purposes, we used HeLa cells that stably expressed the nucleolar protein fibrillarin fused to the green fluorescent protein (GFP) and U2OS cells stably transfected with a GFP-G3BP1 construct that decorates cytoplasmic stress granules (SGs). SGs are cyto-plasmic foci accumulating under various stressful conditions, such as those potentially elicited by the incubation of cells with nanoparticles, and mainly consisting of translationally inactive mRNAs.[30,31]

In both HeLa and U2OS cells, the nanoparticles appeared concentrated in small cytoplasmic foci (Fig. 4 and S5†), which were excluded from the nucleus and nucleolus (Fig. 4A and B and S5†), and did not co-localize with SGs (Fig. 4C). Strikingly, the nanoparticles were nearly systematically polarized in the cytoplasm to one side of the nucleus. This localization, which is

Cool-LED illuminator and a Roper HQ2 camera. (i) DIC (differential interference contrast). The arrowhead points to granules, easily distinguishable in the DIC image and corresponding to NPs. Scale bar = 20 μm. (ii) NPs in red and nucleoli in green. (C) U2OS cells stably expressing GFP-G3BP1. DNA (DAPI) in blue, SGs in green, and NPs in red. Images acquired at 100× with a spindisc confocal microscope mounted with a Yokogawa head and a Roper HQ2 camera.

highly reminiscent of perinuclear membrane-bound organelles, suggested that TEPSA–Rh–PEG NPs are captured by endocytosis, ending up in formation of lysosomes. To test this possibility directly, we performed co-localization studies by immunofluorescence using antibodies specific to EEA1 to detect early endosomes (Fig. 5A). In addition, we used lysotracker staining for lysosomal identification (Fig. 5B). Following 2 days of incubation, we observed some level of co-localization (3.6%) of NPs with early endosomes and a very important (94.7%) co-localization of NPs with the lysosomal compartment (Fig. 5). These observations confirmed our hypothesis.

Finally, we established the extent to which the nanoparticles are transmitted between mother and daughter cells following mitosis. To this end, we performed live-cell imaging and we precisely quantitated the amounts of NPs partitioned between the progenies (Fig. 6). We concluded that following mitosis, the NPs redistribute rather homogeneously with a calculated average ratio over 50 mitotic events of 1.1 between the daughter cells. Furthermore, and in agreement with our observation that NPs are nontoxic to cultured cells, we did not detect any influence of the presence of NPs on cell division. The average doubling time and average time to complete mitosis of 22 h and 69 min, respectively, in our HeLa cell line were largely unaffected by the presence of the NPs (data not shown). Finally, we observed that NPs are stably incorporated into cells, since they were still detected up to 4 days following initial incubation.

Small animal imaging

For *in vivo* imaging experiments, the TEPSA–Rh–PEG NPs were injected intravenously *via* the tail vein into a tumor-bearing DBA–2 mouse and into healthy mice derived from the BalbC strain. As the NPs are expected to have long circulation time properties, the injected animals were observed by MRI for 2 hours just after injection and then at defined periods several days post-injection. MR signal darkening was observed in the liver, coherent with the usual uptake of the iron oxide nanoparticles in this organ, mainly by macrophages (Kupffer cells).[32] This negative contrast in the liver persisted for several days (until 3 days post-injection), in accordance with the role of iron
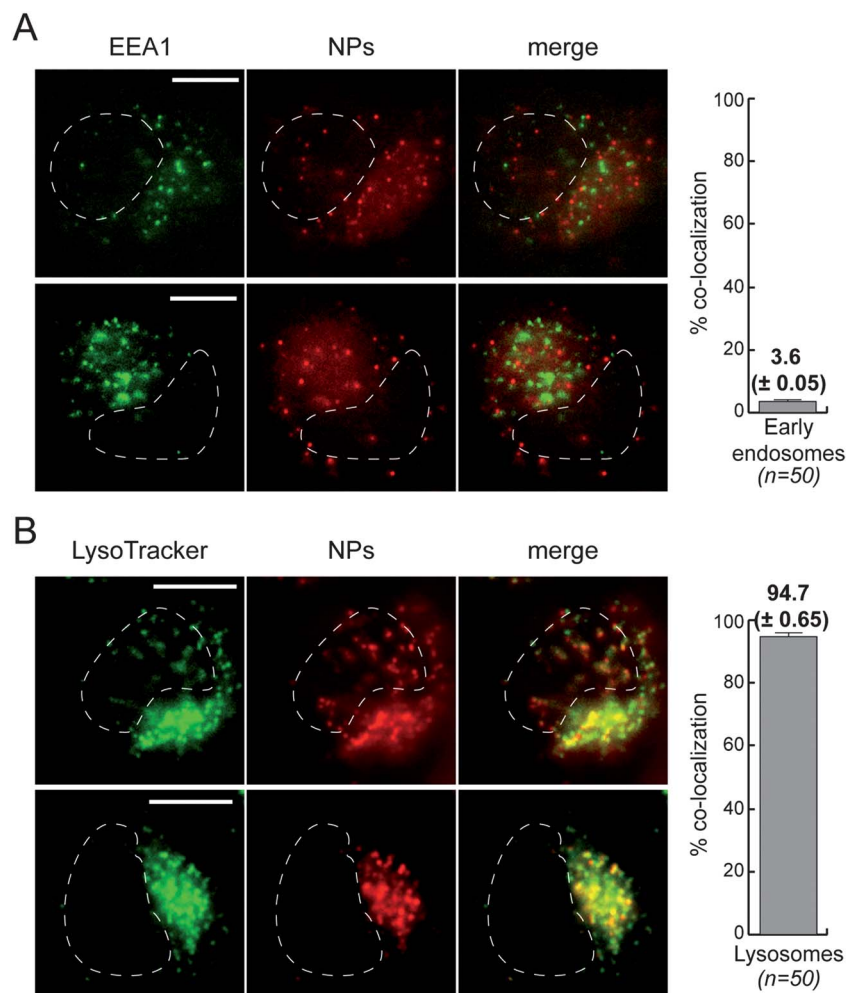

Fig. 5 NPs are captured by cells by endocytosis, ending up in endosomes and lysosomes. HeLa cells were incubated with 50 µg ml^{-1} Fe equivalent of NPs for 2 hours, the excess of NPs washed out, and cells cultured for 3 days. Cells were fixed and processed for immunostaining with an anti-EEA1 antibody (A) or stained with lysotracker (B). Cell nuclei are represented by a dashed line. The % of co-localization of NPs with endosomes (EEA1) and lysosomes (lysotracker) are indicated.
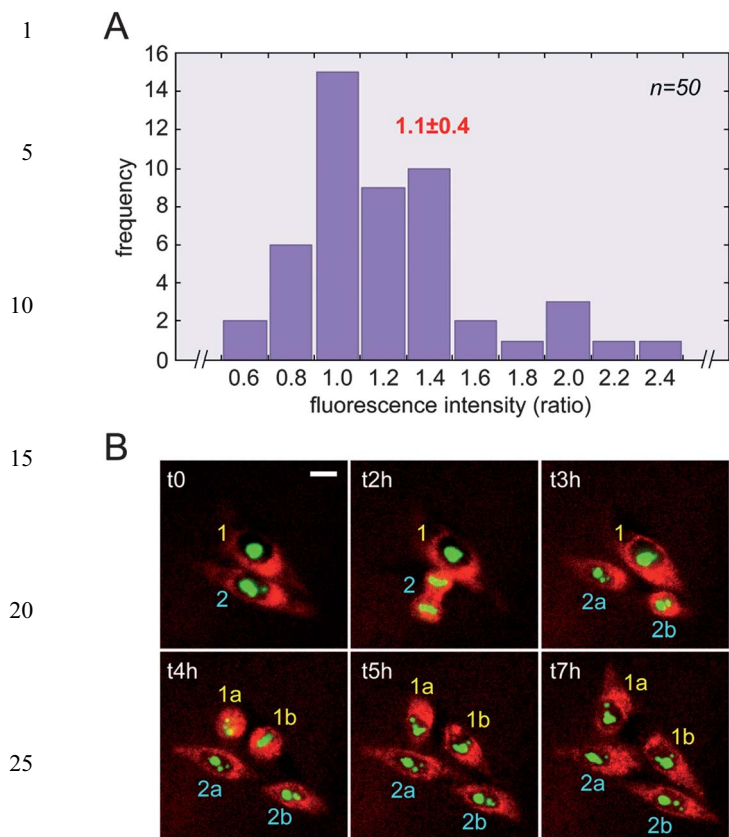
Fig. 6 NPs are equally distributed between daughter cells following mitosis. HeLa cells stably expressing fibrillarin were incubated with 50 μg ml^{-1} Fe equivalent of NPs for 2 hours, the excess NPs were washed out, and cells were followed by live cell imaging for 2 days. (A) 50 mitotic events were monitored and the ratio of rhodamine (corresponding to NPs) fluorescence between the two daughter cells established. (B) As an illustration, two cells are shown. The cell labeled as 1 has been divided by time point 4 hours into cells 1a and 1b showing equal distribution of the NP red fluorescence. This is similar for the cell labeled as 2, which has been divided into cells 2a and 2b by time point 3 hours.

oxide nanoparticle metabolization played by the liver (Fig. 7A and B). MR imaging was also focused on the urinary bladder, which showed signal darkening over an observation time of 2 hours, suggesting that some injected USPIO are small enough (approximately 10 nm diameter) to undergo renal filtration.[33] Signal darkening was observed in the blood circulation, as illustrated in coronal images by the hypo-contrasted *vena cava* 15 minutes after injection of the nanoparticles in a BalbC strain-derived mouse (Fig. 7D). In the DBA–2 mouse, as an illustrative main blood vessel, the *aorta* appears black-colored within the direct post-injection observation period (2 hours). This vessel returned to normal within 3 days of repeated imaging sessions with an MRI sequence that was not deeply T_2-weighted for better visualization of USPIO-induced liver signal decrease at 9.4 T (Fig. 7A). In more T_2-weighted MR images, the *aorta* maintained a darker aspect until the last observation day (day 3), attesting to the long-circulation properties of the USPIO (Fig. 7B). Interestingly, the presence and persistence of USPIO in the intravascular compartment allowed for the depiction of

tumor blood vessels in the subcutaneously implanted *mastocytoma*. Furthermore, a slow phenomenon of USPIO retention at the level of those leaky blood vessels took place within few days post-injection, known as the enhanced permeability and retention (EPR) effect (Fig. 7C).[34] With adequate PEG-related stealthiness, the here-presented USPIO could thus be an interesting MRI tool for "classical" macrophage uptake applications in healthy *versus* metastatic parts of the liver/lymph nodes, or for MRI of macrophage-invaded inflammatory tissues.[35–39] With their blood pool and steady-state susceptibility contrast agent properties, these USPIO could also be used for MRI analysis of the intravascular compartment (vessel size index and blood volume fraction) in tumor or brain perfusion studies.[40,41] At a longer time scale, the usefulness of the EPR effect that USPIO can undergo in tumor blood vessels can be of great interest for cancer therapy applications.[34] The use of such USPIO for molecular imaging after conjugating them to target-specific ligands can also be envisaged.[42]

Using *in vivo* optical imaging, the USPIO-injected tumor-bearing animal was compared to another tumor bearing animal that did not receive USPIO. Results suggested that the amount of USPIO in specific tissues was sufficient for its fluorescent signal to be detected in the whole tumor-bearing mouse. Indeed, the fluorescent signal (λ_{exc}: 540 nm; λ_{emi}: 615 nm; λ_{bckg}: 480 nm) located at the level of the liver of the USPIO-injected mouse could be observed, as illustrated in Fig. 8A, 48 h after i.v. administration of the rhodamine-conjugated nanoparticles. This reflects the liver uptake of USPIO. In the lower part of the mouse abdomen, the urinary bladder gives a fluorescent signal mostly due to flavins (Fig. 8A).[43] The tumor also showed fluorescence under the same imaging conditions (Fig. 8B). It has to be noted that for each mouse most of the fluorescent signal was collected from the necrotic coagulum (dried blood) at the top of the tumor. Nevertheless, the USPIO-injected mouse showed a fluorescent signal that did not appear as only restricted to the necrotic tumor top, potentially reflecting the blood vessel content and the EPR effect allowed by the leaky tumor vasculature that leads to retention of the USPIO in tumor tissue surrounding the vessels. *Ex vivo* examination of the liver and of the tumor (turned upside down regarding its *in situ* position to avoid dried blood fluorescent signal) by optical imaging 72 hours post-injection confirmed the *in vivo* results (Fig. 8C and D). The here-presented USPIO can thus be detected in tissues by MRI and fluorescence imaging, which qualifies them as bimodal imaging contrast agents.[44]

Conclusions

In this study, we demonstrated that TEPSA–Rh–PEG nanoparticles are potential bimodal contrasting agents. We produced thinly coated stable iron oxide nanoparticles characterized by a very narrow size distribution. The presence of carboxylic functions on the surface of our NPs allowed us to tag them with a derivative of rhodamine, generating a contrast agent that we showed has great potential for preclinical bimodal imaging applications. Among others, the persistence of USPIO in the intravascular compartment allowed for the depiction of
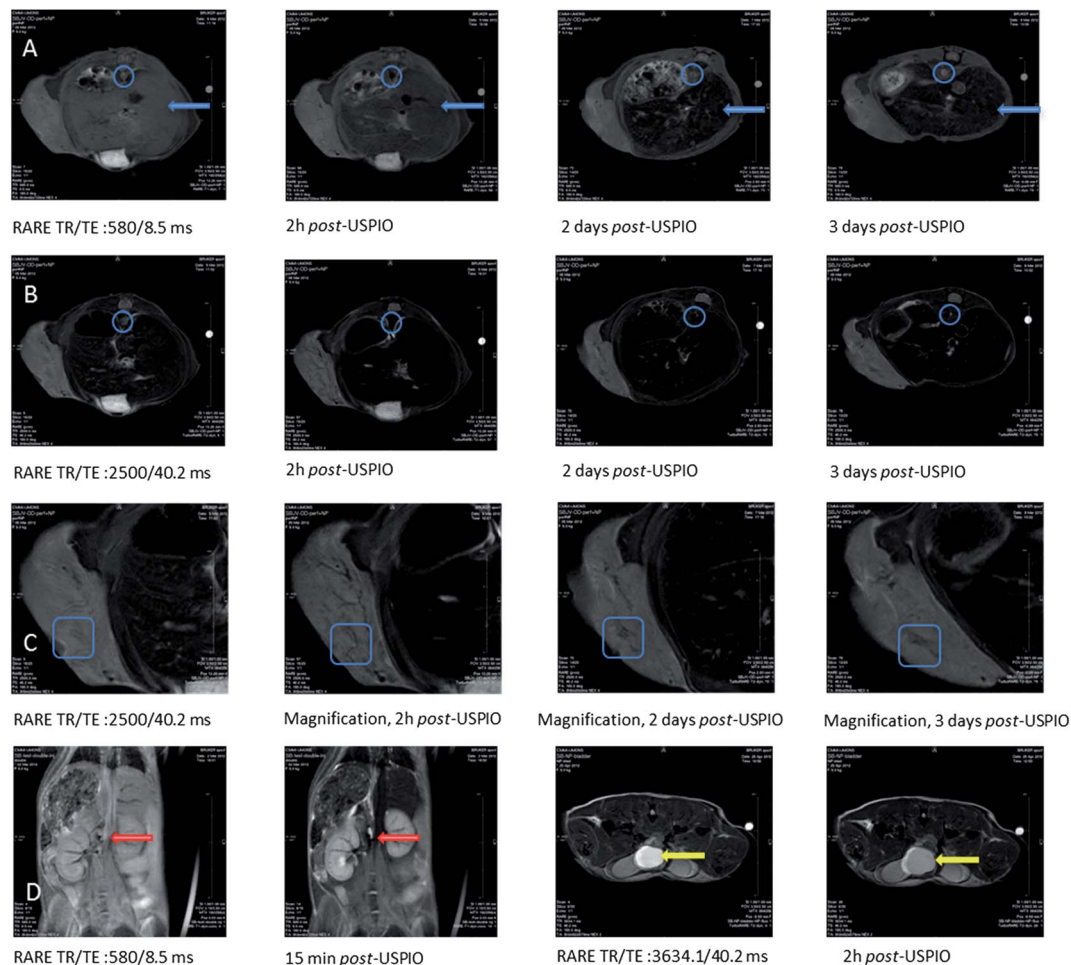
Fig. 7 Illustration of *in vivo* MRI data collected on mice with USPIO injected i.v. at a dose of 120 micromoles Fe per kg. Axial MRI slices in the abdomen of a mouse before, 2 h, 2 and 3 days after injection of USPIO (weak T_2-weighting (row A) and stronger T_2-weighting (row B)); the blue arrow points at the liver and the blue circle is drawn around the aorta. Magnification of the subcutaneous mastocytoma of axial slices from row B; a blue frame surrounds a tumor region containing blood vessels in which USPIO undergo the EPR effect (row C). Coronal MRI slice of a mouse before and 15 minutes after i.v. USPIO injection; the red arrow points at the vena cava (row D, left). Axial MRI slice of a mouse before and 2 h after injection of USPIO; the yellow arrow points at the urinary bladder (row D, right).
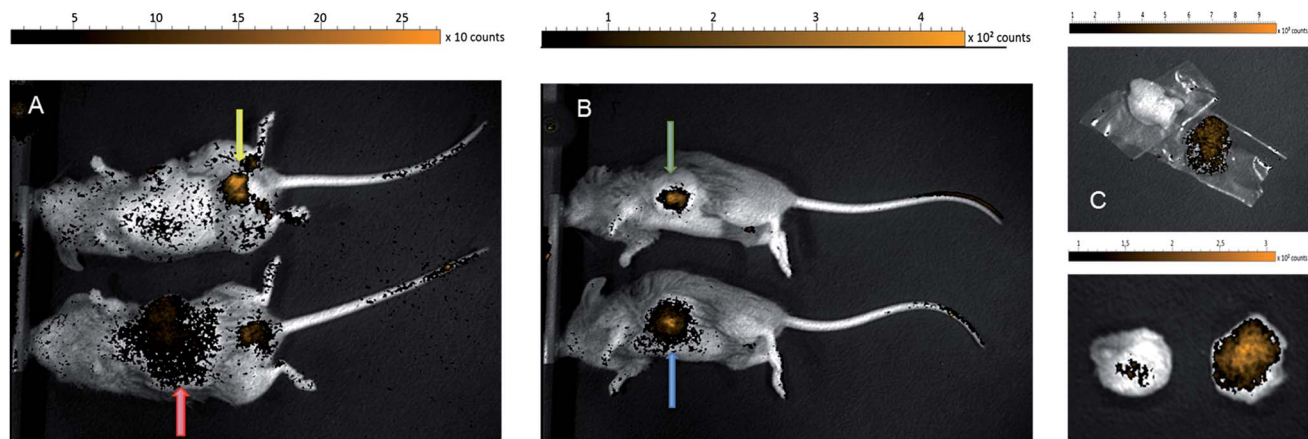

Fig. 8 Optical fluorescent images (540 nm$_{exc}$; 615 nm$_{emi}$; 480 nm$_{bckg}$) 120 micromoles Fe per kg in a *mastocytoma* bearing mouse (bottom in A and B), compared to a non-injected control mouse (top). The control mouse's urinary bladder (yellow arrow) is labeled owing to the presence of flavins. For the USPIO-injected mouse, fluorescent signals from the liver *in vivo* (A, red arrow) and *ex vivo* (C), and from the tumor *in vivo* (B, blue arrow) and *ex vivo* (D) were collected. *In vivo* images: 48 h post-injection (yellow arrow: urinary bladder, green arrow: necrotic coagulum) and *ex vivo* images: 72 h post-injection.

This journal is © The Royal Society of Chemistry 2014

J. Mater. Chem. B, 2014, **xx**, 1–11 | **7**

tumor blood vessels in the subcutaneously implanted *mastocytoma*. With adequate PEG-related stealthiness, the here-presented USPIO could thus be an interesting MRI tool for the analysis of the intravascular compartment (vessel size index and blood volume fraction) in tumor or brain perfusion studies that would benefit from their blood pool and steady-state susceptibility contrast agent properties.

Finally, *in cellulo* studies provided interesting information about the internalization pathways and cellular distribution upon mitosis of the here-presented USPIO. We found that cultured human cells naturally uptake these NPs at an optimal concentration of 50 µg ml^{-1} Fe, that the NPs accumulate in lysosomes indicating that they are entering cells by endocytosis, and that the NPs are equally partitioned between daughter cells following mitosis. We also showed that these nano-systems are non-toxic to mouse and human cultured cells as they do not impact the average time for mitosis completion, the doubling time, or cell viability.

Grafting a specific vector in order to obtain a probe for molecular imaging studies appears as an exciting research axis to develop. Previous studies performed in our laboratory have already highlighted specific tags that are able to target, among others, the inflammation process or apoptosis.

Experimental section

Nanoparticle preparation

Materials. Ferric chloride solution (FeCl$_3$, 45%), ferrous chloride tetrahydrate (FeCl$_2$·4H$_2$O, >99%), and sodium hydroxide were purchased from Fluka (Belgium). Diethyleneglycol (DEG), *O*-(2-aminoethyl)-*O*′-methylpolyethyleneglycol (750 g mol^{-1}), *N*-(3-dimethylaminopropyl)-*N*′-ethylcarbodiimide hydrochloride (EDC), *N*-Boc-1,4-butanediamine, dimethylformamide (DMF), acetone, diethylether, and anhydrous tetrahydrofuran (THF) were purchased from Sigma-Aldrich (Belgium). 3-(Triethoxysilyl)propyl succinic anhydride was purchased from ABCR (Germany). Lissamine rhodamine B sulfonyl chloride was purchased from Acros Organics (Belgium). All the materials mentioned above were used without further purification. Membranes (MWCO = 30 000) for ultrafiltration were purchased from Millipore (USA).

Characterization techniques. Transmission electron microscopy (TEM) was used to obtain detailed morphological information on the samples and was carried out using a Fei Tecnai 10 microscope (Oregon, USA) operating at an accelerating voltage of 80 kV. The samples were prepared by placing a drop of diluted suspension of iron oxide nanoparticles on a copper-grid (300 mesh), allowing the liquid to dry in air at room temperature. The statistical analysis of the TEM images was performed by iTEM (Germany) on multiple images for each sample. The mean diameter, the standard deviation, and the polydispersity index (PDI) were calculated by measuring the particle diameter. The number of nanoparticles counted ranged from 500 to 700. Measurements of the size distribution and the zeta potential of the nanoparticles suspended in aqueous medium were performed on a Zetasizer Nano ZS (Malvern Instruments, United Kingdom) using laser He–Ne (633 nm). The zeta potential was determined directly in

solution containing NaCl (0.01 mM). The pH of the aqueous suspension containing the particles was adjusted by adding 0.1–0.001 mM HNO$_3$ or NaOH solution. Nuclear Magnetic Relaxation Dispersion (NMRD) profiles were recorded with a field cycling relaxometer (STELAR, Mede, Italy) measuring the longitudinal relaxation rates (R_1) in a magnetic field range extending from 0.24 mT to 1 T. The temperature of the samples was adjusted to 37 °C with a precision of 0.1 °C. The theoretical adjustment of the NMRD profiles was performed with classical relaxation models.[18–20] Longitudinal (R_1) and transverse (R_2) relaxation rate measurements at 0.47 and 1.41 T were obtained on Minispec mq 20 and mq 60 spin analyzers (Bruker, Germany), respectively. The relaxation rates were measured as a function of the iron molar concentration at 0.47 and 1.41 T in order to calculate the r_1 and r_2 relaxivities (defined as the enhancement of the relaxation rate of water protons in 1 mmol l^{-1} solution of contrast agents). The relaxivities were calculated as the slope of relaxation rate (R_i^{obs}) *versus* iron concentration according to the equation:

$$R_i^{\mathrm{obs}} = \frac{1}{T_i^{\mathrm{obs}}} = r_i[\mathrm{Fe}] + \frac{1}{T_i^{\mathrm{dia}}}$$

r_i being the relaxivities and T_i^{dia} being the proton relaxation times in aqueous solutions without nanoparticles.

The total iron concentration was determined by measuring the longitudinal relaxation rate R_1 according to the method previously described.[21] Briefly, the samples were mineralized by microwave digestion (MLS-1200 Mega, Milestone, Analis, Belgium) and the R_1 value of the resulting solutions was recorded at 0.47 T and 37 °C, which allowed the determination of iron concentration using the equation:

$$[\mathrm{Fe}] = (R_1^{\mathrm{sample}} - R_1^{\mathrm{diam}}) \times 0.0915$$

where R_1^{diam} (s^{-1}) is the diamagnetic relaxation rate of acidified water (0.36 s^{-1}) and 0.0915 (s mM) is the slope of the calibration curve.

The emission spectra were recorded at room temperature on a Perkin Elmer LS 55 spectrofluorimeter (Perkin Elmer, USA). The excitation and emission slits were set at 10 nm while the scanning rate was set at 1200 nm min^{-1}. ^{1}H-NMR spectra were obtained using a Bruker AMX instrument (300 MHz), and chemical shifts (δ) are given in ppm using tetramethylsilane (TMS) as an internal reference. The following abbreviations are used: br for broad, s for singlet, d for doublet, t for triplet, q for quadruplet, and m for multiplet. IR spectra were recorded on a Perkin Elmer FTIR 1760K (Perkin Elmer, USA).

Synthesis of iron oxide cores. Magnetite nanoparticles (NPs) were prepared by co-precipitation of iron salts in DEG according to a protocol previously described.[22] Briefly, a mixture of ferrous chloride tetrahydrate salt (45 mmol; 8.9 g) and ferric chloride (45%; 37 mmol; 9.1 ml) in DEG (250 ml) was heated at 170 °C under a nitrogen atmosphere and under stirring. After 15 min at that temperature, solid sodium hydroxide (15 g) was added in order to prevent any dilution. The solution was stirred for 1 h at 170 °C. The mixture was then cooled and the magnetic particles were isolated from the solution by magnetic

8 | *J. Mater. Chem. B*, 2014, **xx**, 1–11

This journal is © The Royal Society of Chemistry 2014

decantation ($B_0 = 0.5$ T), after which the black precipitate was washed five times with an aqueous solution of nitric acid (200 ml, 1 M). Finally, magnetite was dispersed in deionized water, sonicated (45 minutes), and centrifuged (16 500g; 45 min) to remove aggregates.

Preparation of TEPSA-modified magnetic nanoparticles. In a first step, the as-obtained suspension of NPs (20 ml; [Fe] = 250 mM) was diluted with dimethylformamide (50 ml) and water was eliminated under reduced pressure. TEPSA (25 mmol; 7.1 ml) was then slowly added to the nanoparticle dispersion in DMF; water was then added (4.3 ml), followed by an aqueous solution of TMAOH (1 M; 2.5 mmol; 2.5 ml) at room temperature and under stirring. The solution was heated to 100 °C for 24 h under continuous stirring. The magnetic nano-objects were collected after pouring the suspension in an acetone–diethylether mixture and magnetic decantation. After washing with acetone, the black precipitate was dispersed in water and purified by membrane filtration (membrane cut-off: 30 kDa) and finally centrifuged (16 500g; 45 minutes). The content of carboxylic moieties was estimated by conductimetric titration, yielding a molar ratio of 2.6 mol% acidic functions compared to the total iron content.

Rhodamine derivatization. N-Boc-1,4-butanediamine (1.5 mmol; 287 µl) was added to a solution of lissamine rhodamine B sulfonyl chloride (0.5 mmol; 289 mg) in anhydrous tetrahydrofuran (70 ml), under stirring and a nitrogen atmosphere. The solution was heated under refluxing conditions overnight. After cooling, the purple solid was filtered and washed with diethylether. The precipitate was solubilized in a trifluoroacetic acid–dichloromethane mixture (30/70; 5 ml) and stirred for 30 minutes at room temperature. After evaporation of dichloromethane under reduced pressure, diethylether was added in order to induce the precipitation of the product. The purple solid obtained after filtration was used without further purification.

^{1}H-NMR (DMSO-d_6): δ (ppm): 8.42 (1H, s); 7.94 (1H, d, $J = 9$ Hz); 7.5 (1H, d, $J = 9$ Hz); 6.98 (6H, m); 3.64 (10H, m); 2.88 (2H, t, $J = 6$ Hz); 1.56 (4H, m); 1.21 (12H, t, $J = 5$ Hz).

HRMS (ESI-ToF) M^+ $C_{31}H_{41}N_4O_6S_2$ measured: $m/z = 629$.

Synthesis of rhodamine B-labeled magnetic nanoparticles. A small amount of trifluoroacetate sodium salt (4 µmol; 3 mg) was added to an aqueous dispersion of TEPSA-modified nanoparticles (150 mM in iron; 5 ml) in the presence of N-(3-dimethylaminopropyl)-N′-ethylcarbodiimide hydrochloride (50 µmol; 10 mg) as a coupling agent at pH 7.5. After one night under stirring, the ferrofluid was purified by membrane filtration (membrane cut-off = 30 000 kDa) and finally centrifuged (16 500g; 40 minutes). In order to ensure the colloidal stability of the as-prepared particles, O-(2-aminoethyl)-O′-methylpolyethyleneglycol (120 µmol; 90 mg) was added to the ferrofluid in the presence of EDC (200 µmol; 38 mg). The pH was then adjusted to 7.5 and the mixture was stirred at room temperature. After 15 hours of reaction, the suspension was purified by membrane filtration (membrane cut-off = 30 kDa) until no fluorescence could be detected in the supernatant.

In cellulo and microscopy studies

Cell lines and cell culture. The HeLa cell line used in this work was purchased from the NIH AIDS Reagent Program. The FIB364 cell line was derived from HeLa and stably expresses fibrillarin-GFP (a kind gift from Prof. D. Hernandez-Verdun, Institut Jacques Monod, Paris). The H2B–GFP HeLa cell line was a gift from Dr. Birthe Farhenkrog (ULB, Université libre de Bruxelles, Belgium). U2OS cells stably expressing the GFP–G3BP1 construct were made available by Prof. P. Anderson (Brigham and Women's Hospital, Boston, USA). Cells were cultured in DMEM (Sigma, D6429) supplemented with FBS (10%) from PAA (A15-101) and Pen–Strep (50 µg ml^{-1}) from Gibco (Ref. 15070) under 5% CO_2 in a humidified incubator. To stimulate the formation of stress granules (SGs), U2OS cells were incubated with 0.5 mM arsenite for 1 hour. For NPs uptake, cells were incubated for 2 hours with NPs at the indicated concentration, the excess NPs washed out, and the incorporation followed for the time indicated.

Microscopy. Cells were observed on Zeiss Imager.Z1 and Axio Observer.Z1 microscopes, driven by MetaMorph (MDS Analytical Technologies, Canada). The fluorescence signal was captured either with a mercury illuminator and a Zeiss AxioCam HRm camera or with a Cool-LED illuminator and a HQ2 camera (Roper, USA). High-resolution images were captured in the confocal mode using a Yokogawa spindisk head and the HQ2 camera with a laser illuminator from Roper (405 nm 100 mW Vortran, 491 nm 50 mW Cobolt Calypso, and 561 nm 50 mW Cobolt Jive). For observation of fixed samples, cells were grown on glass coverslips in a classical culture medium. Cells were then fixed in 2% formaldehyde and washed with PBS. Coverslips were mounted on microscopy slides using mounting medium for fluorescence (Vectashield, Vector labs, USA). For localization of early endosomes by immunofluorescence, fixed cells were permeabilized for 1 h at room temperature in blocking buffer (PBS 5%, BSA 0.3%, and Triton X-100), incubated overnight at 4 °C with the 1st antibody (EEA1-1:1.000 Abcam, UK), washed with the blocking buffer and incubated for 1 h at room temperature with the 2nd antibody (1:1.000 α-mouse, Alexafluor488 Invitrogen). For live-cell experiments, cells were maintained in phenol-red free DMEM (Lonza, Switzerland) supplemented with FBS (10%)/Pen–Strep (50 µg ml^{-1})/ L-glutamine (2 mM)/Na pyruvate (1 mM). Cells were grown in Labtech II chambers and the live conditions were maintained under the microscope using a Chamlide live cell imaging system (Roper). Images were captured every hour in time-lapse mode for 48 h using the Cool-LED illuminator, the HQ2 camera, and the auto-focus controlled automatically by MetaMorph. For lysosome tracking, living cells grown in a Labtech II and containing NPs were treated with LysoTracker Green DND-26 (1:20.000; Life Technologies, Belgium) and directly imaged in epifluorescence. Images were analyzed with Image J.

Small animal imaging

Magnetic resonance imaging. MR imaging was performed on a 9.4 T Biospec (94/20, Bruker, Ettlingen, Germany). One-millimeter thick image slices were collected using a RARE

This journal is © The Royal Society of Chemistry 2014

J. Mater. Chem. B, 2014, xx, 1–11 | 9

sequence. The parameters for global USPIO-related signal decrease visualization were: TR/TE = 580/8.5 ms, RARE factor = 2, MTX = 192×256, FOV = 35×25 (axial) or 31×35 (coronal) mm, 4 averages, and TA = 3 min 43 s, and for more localized USPIO-related T_2 signal decrease they were: TR/TE = 2500–3634.1/40.21 ms, RARE factor = 8, MTX = 384×256, FOV = 35×25 mm, 2–4 averages, and TA = 3 min 53 s to 5 min 20 s. In accordance with the ethical protocol "CMMI-2011-07" of the Center for Microscopy and Molecular Imaging in Gosselies (LA number 1500589), these illustrative and preliminary USPIO-enhanced MR images were recorded in healthy mice derived from the BalbC strain (Charles River, L'Abresle, France) and in mice bearing tumor (with the model developed on the DBA/2 mouse by the team of Prof. Muriel Moser at the Immunobiology Laboratory of the Institute of Molecular Biology and Medicine, ULB-Gosselies) from 18 to 21 days after subcutaneous implantation of 1.5×10^7 P815-C13 mastocytoma cells. All animals were kept anesthetized with 1–1.5% isoflurane in 100% oxygen (0.4 l min^{-1}) delivered through a nosecone and their body temperature was maintained. The respiratory rate was monitored during the entire imaging session. MR images were acquired until 3 days after tail vein injection of the USPIO (120 micromoles Fe per kg).

Optical imaging. Optical imaging was performed using a PhotonImager (Biospace Lab., France). Fluorescence images were collected on tubes containing USPIO and on mastocytoma-bearing mice non-injected or 2 days after injection of the USPIO (120 micromoles Fe per kg i.v. at the 18th day of the mastocytoma), according to the same ethical protocol as for MRI, focusing on the liver and on the tumor after shaving the animals in areas of interest. The mice were kept anesthetized with 1–1.5% isoflurane in 100% oxygen (0.4 l min^{-1}) delivered through a nosecone and their body temperature was maintained. Three days after injection (21st day of the mastocytoma), the animals were euthanized under deep anesthesia and the organs/tissues of interest were collected and directly observed in fluorescence imaging. For *ex vivo* and *in vivo* fluorescence imaging, as well as for acquisition on tubes containing USPIO, excitation was performed at 540 nm and the resulting fluorescent signal was collected from 615 to 900 nm. For *in/ex vivo* experiments, the fluorescent signal was accumulated for 30 s, and a fluorescence background image with the same duration was collected (480 nm excitation) and subtracted from the 615 nm image.

Acknowledgements

Notes and references

1 D. L. J. Thorek, A. K. Chen, J. Czupryna and A. Tsourkas, *Ann. Biomed. Eng.*, 2006, **34**, 23–38.

2 A. K. Gupta, C. Berry, M. Gupta and A. Curtis, *IEEE T. Nanobiosci.*, 2003, **2**, 255–261.

3 Q. A. Pankhurst, J. Connolly, S. K. Jones and J. Dobson, *J. Phys. D: Appl. Phys.*, 2003, **36**, R167–R181.

4 E. Duguet, S. Vasseur, S. Mornet and J. M. Devoisselle, *Nanomedicine*, 2006, **1**, 157–168.

5 S. Laurent, D. Forge, M. Port, A. Roch, C. Robic, L. Vander Elst and R. N. Muller, *Chem. Rev.*, 2008, **108**, 2064–2110.

6 A. K. Gupta, R. R. Naregalkar, V. K. Vaidya and M. Gupta, *Nanomedicine*, 2007, **2**, 23–39.

7 A. K. Gupta and M. Gupta, *Biomaterials*, 2005, **26**, 3995–4021.

8 M. Lattuada, P. Sandkuhler, H. Wu, J. Sefcik and M. Morbidelli, *Adv. Colloid Interface Sci.*, 2003, **103**, 33–56.

9 V. A. Bloomfield, *Biopolymers*, 2000, **54**, 168–172.

10 P. Persson, N. Nilsson and S. Sjöberg, *J. Colloid Interface Sci.*, 1996, **177**, 263–275.

11 S. Mohapatra, N. Pramanik, S. K. Ghosh and P. Pramanik, *J. Nanosci. Nanotechnol.*, 2006, **6**, 823–829.

12 C. Zhang, B. Wangler, B. Morgenstern, H. Zentgraf, M. Eisenhut, H. Untenecker, R. Kruger and F. Kiessling, *Langmuir*, 2007, **23**, 1427–1434.

13 A. K. Boal, K. Das, M. Gray and V. M. Rotello, *Chem. Mater.*, 2002, **14**, 2628–2636.

14 H. T. Song, J. S. Choi, Y. M. Huh, S. Kim, Y. W. Jun, J. S. Suh and J. Cheon, *J. Am. Chem. Soc.*, 2005, **127**, 9992–9993.

15 Y. M. Huh, Y. W. Jun, H. T. Song, S. Kim, J. S. Choi, J. H. Lee, S. Yoon, K. S. Kim, J. S. Shin, J. S. Suh and J. Cheon, *J. Am. Chem. Soc.*, 2005, **127**, 12387–12391.

16 T. Fried, G. Shemer and G. Markovich, *Adv. Mater.*, 2001, **13**, 1158–1161.

17 J.-L. Bridot, D. Stanicki, S. Laurent, S. Boutry, Y. Gossuin, P. Leclère, R. Lazzaroni, L. Vander Elst and R. N. Muller, *Contrast Media Mol. Imaging*, 2013, in press.

18 A. Roch, P. Gillis, A. Ouakssim and R. N. Muller, *J. Magn. Magn. Mater.*, 1999, **201**, 77–79.

19 A. Roch, Y. Gossuin, R. N. Muller and P. Gillis, *J. Magn. Magn. Mater.*, 2005, **293**, 532–539.

20 P. Gillis, F. Moiny and R. A. Brooks, *Magn. Reson. Med.*, 2005, **47**, 257–263.

21 S. Boutry, D. Forge, C. Burtea, I. Mahieu, O. Murariu, S. Laurent, L. Vander Elst and R. N. Muller, *Contrast Media Mol. Imaging*, 2009, **4**, 299–304.

22 D. Forge, A. Roch, S. Laurent, H. Tellez, Y. Gossuin, F. Renaux, L. Vander Elst and R. N. Muller, *J. Phys. Chem.*, 2008, **112**, 19178–19185.

23 C. C. Berry, S. Wells, S. Charles and A. S. G. Curtis, *Biomaterials*, 2003, **24**, 4551–4557.

10 | *J. Mater. Chem. B*, 2014, **xx**, 1–11

This journal is © The Royal Society of Chemistry 2014

24 X. An and Z. Su, *J. Appl. Polym. Sci.*, 2001, **81**, 1175–1181.

25 A. K. Gupta and S. Wells, *IEEE T. Nanobiosci.*, 2004, **3**, 66–73.

26 S. Santra, R. Tapec, N. Theodoropoulou, J. Dobson, A. Hebard and W. Tan, *Langmuir*, 2001, **17**, 2900–2906.

27 I. J. Bruce and T. Sen, *Langmuir*, 2005, **21**, 7029–7035.

28 A. Del Campo, T. Sen, J. P. Lellouche and I. J. Bruce, *J. Magn. Magn. Mater.*, 2005, **293**, 33–40.

29 V. Rerat, S. Laurent, C. Burtea, B. Driesschaert, V. Pourcelle, L. Vander Elst, R. N. Muller and J. Marchand-Brynaert, *Bioorg. Med. Chem. Lett.*, 2010, **20**, 1861–1865.

30 P. Anderson and N. Kedersha, *Nat. Rev. Mol. Cell Biol.*, 2009, **10**, 430–436.

31 P. Anderson and N. Kedersha, *Curr. Biol.*, 2009, **19**, R397–R398.

32 P. Bourrinet, H. H. Bengele, B. Bonnemain, A. Dencausse, J. M. Idee, P. M. Jacobs and J. M. Lewis, *Invest. Radiol.*, 2006, **41**, 313–324.

33 J. E. Zuckerman, C. H. J. Choi, H. Han and M. E. Davis, *Proc. Natl. Acad. Sci. U. S. A.*, 2012, **109**, 3137–3142.

34 V. P. Torchilin, *AAPS J.*, 2007, **9**, E128–E147.

35 J. V. Jokerst, T. Lobovkina, R. N. Zare and S. S. Gambhir, *Nanomedicine*, 2011, **6**, 715–728.

36 M. G. Harisinghani, J. Barentsz, P. F. Hahn, W. M. Deserno, S. Tabatabaei, C. H. van de Kaa, J. de la Rosette and R. Weissleder, *N. Engl. J. Med.*, 2003, **348**, 2491–2499.

37 R. Azoulay, P. Olivier, O. Baud, C. Verney, R. Santus, P. Robert, P. Gressens and G. Sebag, *J. Magn. Reson. Imag.*, 2008, **28**, 1046–1052.

38 C. Corot, K. G. Petry, R. Trivedi, A. Saleh, C. Jonkmans, J. F. Le Bas, E. Blezer, M. Rausch, B. Brochet, P. Foster-Gareau, D. Balériaux, S. Gaillard and V. Dousset, *Invest. Radiol.*, 2004, **39**, 619–625.

39 N. Karabulut and N. Elmas, *Diagn. Interv. Radiol.*, 2006, **12**, 22–30.

40 N. Pannetier, B. Lemasson, T. Christen, M. Tachrount, I. Troprès, R. Farion, C. Segebarth, C. Rémy and E. L. Barbier, *NMR Biomed.*, 2012, **25**, 218–226.

41 G. Gambarota, W. Leenders, C. Maass, P. Wesseling, B. van der Kogel, O. van Tellingen and A. Heerschap, *Br. J. Cancer*, 2008, **98**, 1784–1789.

42 S. Laurent, S. Boutry, I. Mahieu, L. Vander Elst and R. N. Muller, *Curr. Med. Chem.*, 2009, **16**, 4712–4727.

43 M. J. P. Leiner, M. R. Hubmann and O. S. Wolfbeis, *Anal. Chim. Acta*, 1987, **198**, 13–23.

44 R. Joshi, V. Feldmann, W. Koestner, C. Detje, S. Gottschalk, H. A. Mayer, M. G. Sauer and J. Engelmann, *Biol. Chem.*, 2013, **394**, 125–135.

This journal is © The Royal Society of Chemistry 2014

J. Mater. Chem. B, 2014, **xx**, 1–11 | 11